THE HL-LHC BEAM GAS VERTEX MONITOR - PERFORMANCE AND DESIGN OPTIMISATION USING SIMULATIONS

B. Kolbinger*, H. Guerin[1], O. R. Jones, T. Lefevre, J. W. Storey,
A. Salzburger, R. Veness, C. Zamantzas, CERN, Geneva, Switzerland
S. M. Gibson, R. Kieffer, Royal Holloway, University of London, Surrey, UK
[1]also at Royal Holloway, University of London, Surrey, UK

Abstract

The Beam Gas Vertex (BGV) instrument is a novel non-invasive beam profile monitor and part of the High Luminosity Upgrade of the Large Hadron Collider (LHC) at CERN. Its aim is to continuously measure emittance and transverse beam profile throughout the whole LHC cycle, which is currently not possible using a single device. The BGV consists of a gas target and a forward tracking detector to reconstruct tracks and vertices resulting from beam-gas interactions. The beam profile is inferred from the spatial distribution of the vertices, making it essential to achieve a very good vertex resolution. Extensive simulation studies are being performed to provide a basis for the design of the future BGV. The goal of the study is to ascertain the requirements for the tracking detector and the gas target within the boundary conditions provided by the feasibility of integrating them into the LHC. This contribution will focus on the simulations of the forward tracking detector. Based on cutting-edge track and vertex reconstruction methods, key parameter scans and their influence on the vertex resolution will be discussed.

INTRODUCTION

Understanding the evolution of beam profile and size throughout the whole accelerator cycle of the LHC is of great importance for the optimisation of emittance, and hence luminosity. The BGV device is foreseen to provide an independent, continuous, non-invasive, and bunch intensity independent measurement of the beam profile throughout the accelerator cycle. Beam-gas collision products stemming from LHC protons, interacting inelastically with the BGV's gas target installed in the path of each circulating beam, are measured via tracking detectors (Fig. 1 A). The beam profile is determined from the spatial distribution of the reconstructed vertices of the collisions.

A BGV demonstrator device has been successfully installed, commissioned and operated during LHC Run 2 [1]. A vacuum pressure bump of 10^{-7} mbar extending over ≈ 2 m was provided by a gas injection system and acted as the target. The forward tracking detector was composed of several planes of scintillating fibres based on the LHCb SciFi detector modules [2]. It successfully demonstrated the feasibility to use inelastic beam gas interactions for beam monitoring. However, due to poor track quality and limited vertexing capabilities, the demonstrator failed to reconstruct the beam profile. A new design is currently under development based

_____
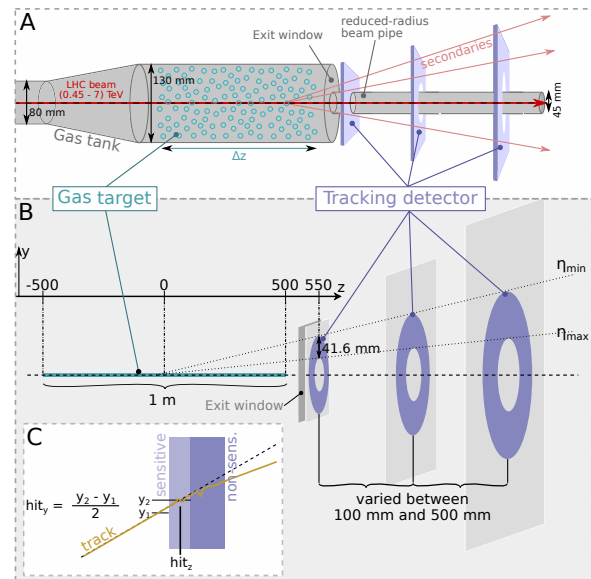* bernadette.kolbinger@cern.ch, corresponding author

Figure 1: A: Sketch of the BGV. B: Generic simulation setup. The interaction region is shown in turquoise. The detector layers are shown in light grey, their active area in purple. The exit window (dark grey) is placed at $z = 545$ mm. C: Z-y cross-section of a detector layer.

on what has been learned from the BGV demonstrator and the results of detailed and complete simulations.

The true beam profile is extracted from the spatial distribution of reconstructed vertices via deconvolution of the vertex response of the BGV system, making the latter the most important figure of merit for the device's performance. However, a precise knowledge of the vertex response is difficult to achieve. It is therefore desirable to keep its width, i.e. the vertex resolution σ_v, low relative to the true beam width σ_b. At the foreseen location of the BGV, the smallest expected beam size will be $\sigma \approx 200$ μm at 7 TeV. Assuming bunches with Gaussian transverse distributions with standard deviations of σ_b and a Gaussian vertex response with a width of σ_v, the following relation arises via deconvolution, error propagation and assuming negligible measurement uncertainty [3]: $\frac{\delta \sigma_b}{\sigma_b} = \frac{\sigma_v^2}{\sigma_b^2} \frac{\delta \sigma_v}{\sigma_v}$, where $\delta \sigma_b$ and $\delta \sigma_v$ denote the absolute beam size and vertex resolution uncertainties. This relation highlights the importance of a small σ_v relative to the beam size and precisely knowing the vertex resolution. Assuming a relative beam size error of ≤ 0.05 (see design specifications listed in Ref. [4]) and $\frac{\delta \sigma_v}{\sigma_v} \leq 0.1$, we arrive at an upper limit for the vertex resolution of $\sigma_v \lesssim 140$ μm.

Vertex resolution and interaction/event rate σ_v depends on various characteristics of the measured tracks corresponding to an interaction, which will henceforth be called an "event". σ_v strongly depends on the number of tracks per event $\sigma_v \propto \frac{1}{\sqrt{N_{tr}}}$, which in turn depends on beam energy, gas species, detector coverage and the distance from the vertex to the detector. The detector coverage is determined by the exit window of the gas tank (see Fig. 1 A), whose maximum radius has been estimated by impedance simulations [4] to be ≈ 65 mm, and the reduced-radius beam pipe downstream of the tank, whose minimum inner radius is 22.5 mm [4] which is given by the required aperture at injection at the BGV location. Furthermore, σ_v is strongly influenced by the track quality, which can be studied via the transverse impact parameter resolution of a single track calculated via [5]:

$$\sigma_{IP}^2 = \sigma_{int,det}^2 + \sigma_{MS}^2 \qquad (1)$$

The intrinsic detector contribution $\sigma_{int,det}$ is calculated via [6] $\sigma_{int,det}^2 = \frac{\sigma_{res}^2}{N+1} + \frac{\sigma_{res}^2}{N+1}\frac{12N}{N+2}\frac{x^2}{L^2}$, where σ_{res} is the spatial resolution, N the number of detector layers, x the distance from the vertex to the centre of the detector and L the detector's total length. This highlights the importance of σ_{res} and the length of the detector for σ_{IP}. The contribution from multiple scattering in the materials is determined via $\sigma_{MS} = \sqrt{d^2\theta_0^2}$, with the distance d from the scattering plane to the vertex and the multiple scattering angle θ_0 (see Ref. [7] for the formula), which depends on the radiation length of the material and the momentum of the particle. In the calculations discussed later, the multiple scattering contributions of the first detector layer and the exit window are included. The first results of the BGV performance study via simulations using a generic geometry are presented in the next section. The goal is to use this general setup to ease navigation of the BGV's extensive parameter space and to efficiently identify the impact of design parameter and verify that there are no showstoppers. Once the dependence of σ_v on BGV and event attributes is known, the rate of events with a sufficiently high vertex resolution can be estimated. The total rate of inelastic beam-gas collisions per proton bunch is calculated via $R_{inel} = f_{rev} N \sigma_{p\text{-gas}}^{inel} \rho_{gas} \Delta z$, where $f_{rev} = 11245$ Hz denotes the revolution frequency of the bunches, $N = 2.2 \times 10^{11}$ [8] the nominal number of protons per bunch after the high luminosity upgrade of the LHC, $\sigma_{p\text{-gas}}^{inel}$ the inelastic cross-section of the interaction, ρ_{gas} the gas density and Δz the length of the gas in the direction of the beam. Considering gas interactions with protons at the LHC injection energy of 450 GeV (representing the case where the fewest secondaries are created compared to interactions at higher beam energies), a neon gas with a pressure of 10^{-7} mbar and $\Delta z = 1$ m, leads to $R_{inel} = 147$ Hz.

SIMULATION SETUP AND ANALYSIS

The first step in the simulation chain is the creation of the secondaries from beam-gas collisions via CRMC [9], an interface which allows access to several hadronic genera-

tors, see Ref. [4]. The resultant HepMC file [10] is read-in by Geant4 [11] which simulates the interaction of the secondaries with the BGV setup. The simulated information such as position, momenta, etc. of secondaries, as well as the simulated detector hits are saved by the Geant4 model. Figure 1 C demonstrates how the hits are determined from the Geant4 particle tracks. Subsequently, tracks and vertices are reconstructed as discussed in the following sections. Finally, the beam profile is determined by deconvolution of the resultant vertex distribution and vertex response, which will not be addressed by this paper.

Simulation geometry and conditions The generic BGV geometry is shown in Fig. 1 B. For the results presented here, 500 000 proton-neon collisions are simulated via the hadronic generator DPMJET 3.06 [12] using a beam energy of 450 GeV. Simulation results with higher beam energies will be discussed in a future and more detailed publication. The longitudinal spread of proton-neon interactions caused by the use of an extended gas volume, is simulated by uniformly distributing the vertices over 1 m along the z direction. Transversely, the vertex distribution is assumed to be Gaussian with a width of 0.5 mm. The exit window is simulated as a square shaped sheet, perpendicular to the z-axis and with a thickness of 0.9 mm (unless otherwise stated). It is entered in the simulation as being made from the same aluminium alloy AA2219 [1] used for the demonstrator tank. This implementation will be updated in future simulations to reflect the actual cone shape of the window with a varying thickness. The current BGV demonstrator has an exit window with a thickness gradient from 0.9 mm (small radii) to 3.2 mm (larger radii). A redesign of the exit window with the goal of lowering its material budget is currently ongoing.

The test setup for the detector consists of three layers of silicon. Each layer is composed of a sensitive material layer, where the hit position is registered for further analysis, and a non-sensitive material behind it, to simulate scattering in the rest of the detector (see Fig. 1 C). The large square shaped detector layers (light grey) allow the use of only one data set by performing subsequent cuts on the pseudo-rapidity η of tracks to simulate different detector sizes, as indicated by the purple discs in Fig. 1 B. In the presented results, the first detector layer covers the entire exit window (23.4 mm $< r < 65$ mm). The size of the subsequent layers is chosen so that they cover the same solid angle with respect to the centre of the gas volume at (0, 0, 0). The distance between the centre of the gas volume and the first detector layer is 550 mm, which showed the highest N_{tr} for 450 GeV protons in previous studies, see Ref. [4]. In order to investigate the influence of the material budget x/X_0 of the tracker, two different detector layer thicknesses w_d are considered: 1 mm (1 % of x/X_0 per layer) of which 300 μm are sensitive, and 0.27 mm (0.29 % of x/X_0 per layer) of which 100 μm are sensitive. Regarding the spatial resolution σ_{res} of the detector, two cases are simulated: (1) $\sigma_{res} = 16$ μm, corresponding to a Si pixel detector such as a Timepix [13] detector with a pixel

TUPP21

pitch of 55 μm, and (2) a lower resolution of $\sigma_{res} = 50$ μm, representing e.g. a GEM tracker [14]. Furthermore, the distance between detector layers d_{det} is scanned in 50 mm steps between 100 mm and 500 mm. Note, that increasing d_{det} also increases the area of the second and third detector layers.

Track and vertex reconstruction In order to reconstruct tracks and the associated primary vertices of the beam-gas interactions, the experiment-independent reconstruction toolkit ACTS (A Common Tracking Software) [15, 16] is used. ACTS is intended for charged particle track reconstruction in high energy particle physics experiments for future colliders, and is based on the ATLAS tracking code. A track is defined as a collection of position measurements (hits) recorded by the detector. Only tracks with a hit in each layer are accepted. The process of track finding, i.e. associating which detector hits belong to which track, is initially omitted and a track finding efficiency of 1 is assumed. The low event rate (event pile-up not likely) and low track multiplicity (see Fig. 2) expected are likely to facilitate finding the tracks with high efficiency. The detector resolution is simulated by Gaussian smearing of the real x and y-hit positions with a certain σ_{res}. The tracks are fitted via ACTS's Kalman Fitter [17]. In order to create initial values for the track parameters, the hits of the first and last detector layer of a track are used. For the particle momentum, used by the Kalman fitting to account for multiple scattering effects, the real information is used. The momenta cannot be estimated from the track curvature since they are straight in the absence of a magnetic field. At a later stage, this will be replaced by an estimation via simulations, e.g. using the correlation of momentum with pseudo-rapidity. Afterwards, the fitted tracks are used to determine the vertex via the Billoir fitter [18]. σ_v can then be determined by comparing the true vertices to the reconstructed vertices, i.e. the residual distributions of the vertex components $r_i = v_{i,\text{fit}} - v_{i,\text{true}}$ with $i = \{x, y, z\}$. An example residual distribution of r_x is shown in Fig. 3. The vertex resolution is extracted by fitting the residual with a sum of two Gaussians, the so-called core and tail Gaussians [19], that are both centred around zero, but have different widths σ_c and σ_t. The underlying reason for this is that σ_v is impacted by the momenta, opening angles etc. of the tracks stemming from the vertices. The contribution of vertices to core and tail are calculated via the core and tail fractions: $f_c = \frac{p_c \sigma_c}{p_c \sigma_c + p_t \sigma_t}$ and $f_t = \frac{p_t \sigma_t}{p_c \sigma_c + p_t \sigma_t}$, where p denotes the amplitudes and σ the widths of the Gaussians. The vertex resolution can then be calculated as the weighted average $\sigma_v = \sqrt{f_c \sigma_c^2 + f_t \sigma_t^2}$. Since the BGV's main purpose is to measure the transverse profile, the following discussion of the vertex resolution is solely focussed on σ_x and σ_y, also summarised as $\sigma_{x,y}$ in the following.

VERTEX RESOLUTION RESULTS

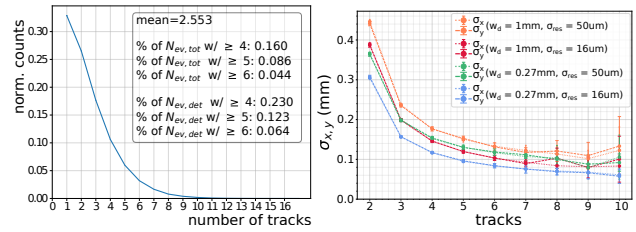In this section, the simulation results of $\sigma_{x,y}$ and their dependence on some key parameters are discussed and compared to calculations of σ_{IP} via Eq. (1). A histogram showing the number of tracks per event registered by the detector can be seen in Fig. 2 (left). The percentage of events with a certain N_{tr} or higher are also listed, e.g. 16 % of all collisions show $N_{tr} \geq 4$. The dependence of $\sigma_{x,y}$ on N_{tr} can be seen in Fig. 2 (right). Here, d_{det} has been fixed to 250 mm and results for detector resolutions $\sigma_{res} = \{16, 50\}$ μm and $w_d = \{1, 0.27\}$ mm are shown. As expected, the vertex resolution improves with higher track numbers. The size of the error bars is calculated via error propagation of the fit errors on σ_c, σ_t, p_c and p_t. They increase with higher N_{tr} due to the lower statistics for a given number of primary events. The vertex resolution starts converging at $N_{tr} \approx 5$ to 6. As expected, the detector with the highest resolution and lowest material budget (blue) shows the best $\sigma_{x,y}$, dropping below 140 μm between 3 and 4 tracks. Furthermore, it can be seen that $\sigma_{x,y}$ of the detector with higher material budget and higher resolution (red), drops quicker than the detector with lower w_d and lower resolution (green).

Figure 2: Left: histogram of N_{tr}. The percentage of total events and events registered by the detector are also listed. Right: $\sigma_{x,y}$ versus N_{tr} for four different detector cases and a fixed number of total events.
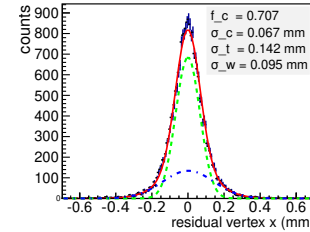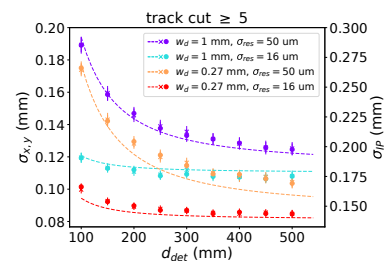

Figure 3: Distribution of r_x of vertices stemming from events with 5 tracks. The red line shows the fit of the sum of two Gaussians via ROOT [20], the green and blue dashed lines show the core and tail Gaussians, respectively.

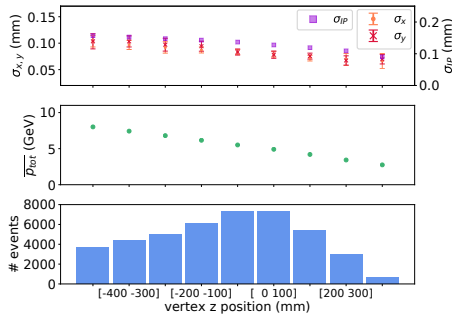Figure 4: $\sigma_{x,y}$ as well as σ_{IP} as a function of d_{det}.

Figure 5: Vertex z position dependence of $\sigma_{x,y}$ and σ_{IP} (top), of the average track momentum (middle), and of the number of events (bottom).
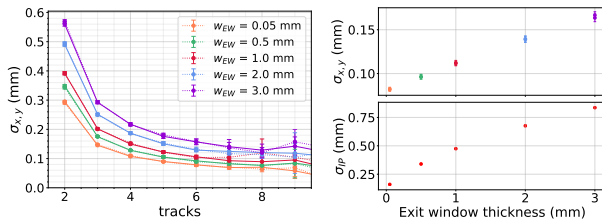

Figure 6: Left: $\sigma_{x,y}$ in dependence of N_{tr} for different window thicknesses. Right: comparison of $\sigma_{x,y}$ (top) and σ_{IP} (bottom) versus w_{EW}.

Figure 4 shows the analysis results of the transverse vertex resolution versus d_{det} for events with $N_{tr} \geq 5$. The calculated results (dashed line) of σ_{IP} (see Eq. (1)), are also presented, for which the average momentum of simulated tracks and a distance of 550 mm between vertices and detector are used. One can see that the behaviour matches the simulation results well. The four colours symbolise detector cases with different material budget and resolution, as noted in the legend of the figure. For $\sigma_{res} = 50$ μm (orange and purple), a significant increase in resolution is observed with d_{det}. On the other hand, for $\sigma_{res} = 16$ μm, the gain in $\sigma_{x,y}$ is less prominent and shows convergence at about 250 mm. These results indicate that a detector with a high spatial resolution such as a Si pixel detector could allow for a more compact detector design.

The dependence of $\sigma_{x,y}$ on the distance between the vertices and the first detector layer, d_{vtx}, is depicted in Fig. 5 (top). A detector with $d_{det} = 250$ mm, $w_d = 0.27$ mm and $\sigma_{res} = 16$ μm is used. The vertices are grouped together in bins with a width of 100 mm, as indicated by the x-axis labels. The data points show the $\sigma_{x,y}$ of events belonging to the same bin and $N_{tr} \geq 5$. As expected from the formulas for σ_{MS} and $\sigma_{int,det}$, the resolution decreases with d_{vtx}. However, this effect is lessened due to the rise of average track momenta with d_{vtx}, see Fig. 5 (middle). Figure 5 (bottom) shows the number of events versus d_{vtx}. Due to the forward nature of the tracks, events closer to the detector are less likely to get registered by the detector. The number of events falls for larger d_{vtx}. Note, that this is dependent on the transverse placement of the detector planes.

Another important parameter is the material budget of the exit window. Figure 6 (left) shows the vertex resolution in dependence of the number of tracks for window thicknesses $w_{EW} = \{0.05, 0.5, 1, 2, 3\}$ mm for a detector with $d_{det} = 250$ mm, $w_d = 1$ mm and $\sigma_{res} = 16$ μm. One can see that the results for $w_{EW} = 1$ mm are fairly close to the idealised case of 0.05 mm for $N_{tr} \geq 5$, and reach $\sigma_{x,y} \leq 140$ μm between 4 and 5 tracks. For $w_{EW} = 2$ and 3 mm, $\sigma_{x,y}$ approaches 140 μm only at 6 and 7 tracks, respectively. The vertex resolution as a function of w_{EW} is shown in Fig. 6 (right). The top plot shows the simulation results ($N_{tr} \geq 5$), the bottom one σ_{IP} for comparison.

The rate of events with sufficient vertex resolution can be calculated as follows. Assuming a tracking detector with $d_{det} = 250$ mm, $w_d = 1$ mm and $\sigma_{res} = 16$ μm, events with $N_{tr} \geq 5$ tracks could be accepted (see Fig. 2 right (red)). Of the 500 000 initial collisions, 69 % have a reconstructable vertex (at least 2 tracks) whereas 7.96% show $N_{tr} \geq 5$. Using the total rate of collisions $R_{inel} = 147$ Hz as calculated in the introduction section, this results in an inelastic rate per bunch of 11.69 Hz of useful events. After an acquisition time of 1 min ($n = 701$ events), the relative statistical error on the bunch width calculated via $\frac{1}{\sqrt{2n-2}}$ [21] would be 2.7 %, which is in the order of magnitude desired by the specifications. However, these first promising estimations are based on an idealised setup and further studies are necessary to incorporate additional effects that impact the vertex resolution, such as a misalignment of the detector. After this first estimation using a generic detector, the next steps will be to add more realism and details to the simulation setup, such as updating the tank exit window, replacing the detector layers by modules based on a chosen technology, etc. In order to increase the rate of useful events, the pressure of the gas target could be increased, however this may be unacceptable for beam operation. A different target gas with a higher atomic number, such as argon, could also be considered to increase the number of tracks per events. Cuts on the z position of the vertex or the track momenta could also increase the resolution or lower the necessary cut on N_{tr}.

SUMMARY & OUTLOOK

The BGV is currently being redesigned for the HL-LHC. First simulation results of an extensive study of the impact of key design parameters on the device's performance have been discussed. Based on the results of the generic BGV setup, design choices of tank shape and detector technology will be made. After a detector technology has been chosen, work on module design and a concrete detector model for the simulation will begin. The first results point towards the possibility of using a compact detector with a high position resolution, like a Si pixel detector.

ACKNOWLEDGEMENTS

REFERENCES

[1] A. Alexopoulos *et al.*, "Noninvasive LHC transverse beam size measurement using inelastic beam-gas interactions," *Physical Review Accelerators and Beams*, vol. 22, no. 4, p. 042 801, Apr. 2019. DOI: `10.1103/PhysRevAccelBeams.22.042801`.

[2] "LHCb Tracker Upgrade Technical Design Report," Feb. 2014. `https://cds.cern.ch/record/1647400`

[3] P. Hopchev *et al.*, "A beam gas vertex detector for beam size measurement in the LHC," *IPAC 2014: Proceedings of the 5th International Particle Accelerator Conference*, pp. 3680–3683, 2014. DOI: `10.18429/JACoW-IPAC2014-THPME175`.

[4] H. Guerin *et al.*, "The HL-LHC Beam Gas Vertex Monitor - Simulations for Design Optimisation and Performance Study," in *presented at the 12th Int. Particle Accelerator Conf. (IPAC'21)*, (Campinas, Brazil), JACoW Publishing, May 2021.

[5] A. Salzburger, "A parametrization for fast simulation of muon tracks in the ATLAS inner detector and muon system," M.S. thesis, Innsbruck U., 2003.

[6] F. Ragusa and L. Rolandi, "Tracking at LHC," *New Journal of Physics*, vol. 9, no. 9, pp. 336–336, Sep. 2007. DOI: `10.1088/1367-2630/9/9/336`.

[7] P. Zyla *et al.*, "Review of Particle Physics," *PTEP*, vol. 2020, no. 8, p. 083C01, 2020. DOI: `10.1093/ptep/ptaa104`.

[8] O. Aberle *et al.*, *High-Luminosity Large Hadron Collider (HL-LHC): Technical design report*, ser. CERN Yellow Reports: Monographs. Geneva: CERN, 2020. DOI: `10.23731/CYRM-2020-0010`.

[9] *CRMC (cosmic ray monte carlo package)*. `https://web.ikp.kit.edu/rulrich/crmc.html`

[10] M. Dobbs and J. B. Hansen, "The HepMC C++ Monte Carlo Event Record for High Energy Physics," CERN, Geneva, Tech. Rep., Jun. 2000.

[11] S. Agostinelli *et al.*, "Geant4 – a simulation toolkit," *NIM A*, vol. 506, no. 3, pp. 250–303, 2003. DOI: `10.1016/S0168-9002(03)01368-8`.

[12] F. W. Bopp, J. Ranft, R. Engel, and S. Roesler, "Antiparticle to particle production ratios in hadron-hadron and *d*-au collisions in the dpmjet-iii monte carlo model," *Phys. Rev. C*, vol. 77, p. 014 904, 1 Jan. 2008. DOI: `10.1103/PhysRevC.77.014904`.

[13] T. Poikela *et al.*, "Timepix3: A 65k channel hybrid pixel readout chip with simultaneous ToA/ToT and sparse readout," *Journal of Instrumentation*, vol. 9, no. 05, pp. C05013–C05013, May 2014. DOI: `10.1088/1748-0221/9/05/c05013`.

[14] M. Titov and L. Ropelewski, "Micro-pattern gaseous detector technologies and rd51 collaboration," *Modern Physics Letters A*, vol. 28, no. 13, p. 1 340 022, 2013. DOI: `10.1142/S0217732313400221`.

[15] X. Ai *et al.*, "A common tracking software project," submitted to *Computing and Software for Big Science* on 25 Jun 2021, 2021. arXiv: `2106.13593 [physics.ins-det]`. `https://arxiv.org/abs/2106.13593`

[16] *Acts on github*, https://github.com/acts-project/acts, Accessed: 2021-08-27.

[17] R. E. Kalman, "A New Approach to Linear Filtering and Prediction Problems," *Journal of Basic Engineering*, vol. 82, no. 1, pp. 35–45, Mar. 1960. DOI: `10.1115/1.3662552`.

[18] P. Billoir and S. Qian, "Fast vertex fitting with a local parametrization of tracks," *Nuclear Inst. and Methods in Physics Research, A*, vol. 311, no. 1-2, pp. 139–150, 1992. DOI: `10.1016/0168-9002(92)90859-3`.

[19] "Performance of tracking and vertexing techniques for a disappearing track plus soft track signature with the ATLAS detector," CERN, Geneva, Tech. Rep., Mar. 2019.

[20] R. Brun and F. Rademakers, "Root – an object oriented data analysis framework," *Nuclear Instruments and Methods in Physics Research Section A: Accelerators, Spectrometers, Detectors and Associated Equipment*, vol. 389, no. 1, pp. 81–86, 1997, New Computing Techniques in Physics Research V. DOI: `10.1016/S0168-9002(97)00048-X`.

[21] L. Lyons, *A Practical Guide to Data Analysis for Physical Science Students*. Cambridge University Press, 1991. DOI: `10.1017/CBO9781139170321`.